3. Experimental Details

This chapter outlines all experimental details connected to time-resolved 2PPE measurements on ice- and ammonia-metal interfaces. It begins with a description of the employed technique, the time-resolved two-photon photoelectron (2PPE) spectroscopy. Then the experimental equipment is presented: Optical setup, UHV components, and electronics. Section 3.3 includes the sample preparation and characterization procedures. Finally, an introduction into the data analysis is given, focusing on the description of electron population dynamics by rate equations.

3.1 Time-Resolved Two-Photon Photoelectron Spectroscopy

Photoelectron (or photo*emission*) spectroscopy is a powerful tool for investigating the electronic structure of solids and their surfaces. Electrons are excited above the vacuum level by absorption of light, where they transfer with a certain probability to vacuum states and leave the sample. Through the detection of their kinetic energy and their emission angle, it is possible to infer the electrons' binding energies and dispersion parallel to the surface. [Hüf95] One-photon photoelectron spectroscopy allows for the investigation of all occupied states from the core levels to valence and conduction bands if appropriate photon energies are chosen.

The application of two-photon photoelectron spectroscopy enables the study of the *unoccupied* band structure in addition. The principle of this *pump-probe* technique [Fau95, Pet98] is shown in Fig. 3.01. By absorption of a first photon ($h\nu_1$, pump) electrons from below the Fermi Level are excited to unoccupied, bound states below E_{vac}. A second, time-delayed photon ($h\nu_2$, probe) excites the

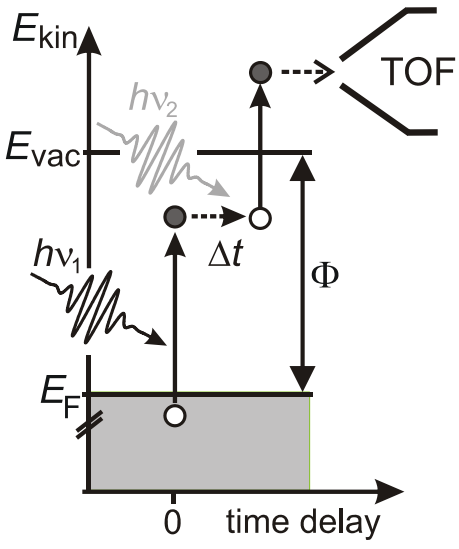

Fig. 3.01: *2PPE Spectroscopy.* The pump pulse excites electrons to bound states above the Fermi Level. A second pulse probes them above the vacuum level and their kinetic energy is analyzed. The pump-probe time delay enables the time resolution.

electron above the vacuum level, where it can be detected by an electron time of flight (TOF) spectrometer. By using ultrashort laser pulses with durations below 100 fs, it is possible to study the dynamics of the electrons in the excited state with femtosecond time resolution. The right choice of photon energies is very important, as the energy of the *pump* pulse needs to be large enough to excite all states of interest, and the *probe* energy has to be sufficiently high to excite the electrons from their intermediate states above the vacuum level. However, if possible, both photon energies should be lower than the sample work function to avoid direct photoemission from electrons below the Fermi Level.

There are several ways for an electron to get from its initial state $|i>$ below E_F via an intermediate state $|n>$ below E_{vac}, to its final state $|f>$ in the vacuum. These pathways depend on the type of the intermediate state. Fig. 3.02 depicts three different excitation mechanisms, two of them are direct (left), one is indirect (right). The first scenario depicts resonant excitation to a "real" intermediate state. The second photon probes the population. If no resonant intermediate state is available, electrons leave the sample directly in a two-photon process, which occurs within the pulse duration. This happens via so-called "virtual" intermediate states, which are not occupied for a finite time (center). The resonant and the non-resonant excitations lead to the same kinetic energy of the photoelectrons. To distinguish between the two cases, the pump photon energy is varied. If a shift of $\Delta h\nu$ is observed in the spectrum, the electrons were excited via virtual states and the spectral signature observed is due to the initial state.[32] If no shift is observed upon photon energy change, the feature corresponds to an intermediate state. Its energy with respect to the vacuum level is well-defined. The third scenario is an indirect process. The electron's intermediate state evolves dynamically, e.g. by secondary scattering processes with other electrons, phonons, or defects. In this case the coherence between the involved states is lost and the electron momentum is changed.

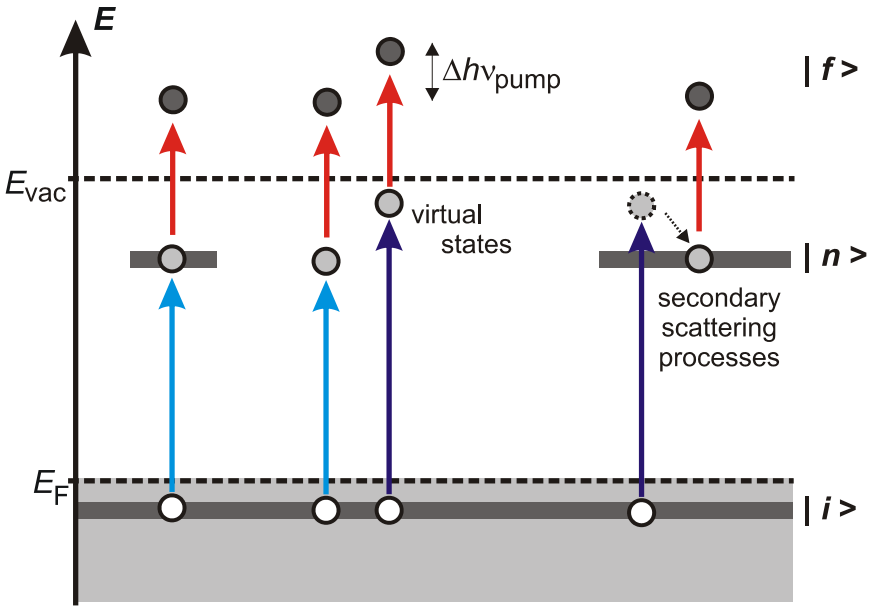

Fig. 3.02: *Excitation Mechanisms.* Resonant and non-resonant passage of the electron. The process can be distinguished by changing the pump photon energy. In the case of an indirect process, which involves secondary scattering events, phase and momentum of the electron is changed.

[32] This situation is for example encountered for the occupied Cu(111) surface state (cf. 2.4.2).

In the present work various combinations of pump-probe photon energies were used. However, all experiments were performed using visible (VIS) and ultraviolet (UV) laser pulses. The time resolution of 2PPE experiments lies at approximately 10% of the laser pulse duration so that a sensitivity of few femtoseconds could be reached. A description of the experimental setup is given in the following section.

3.2 Experimental Setup

The experimental setup employed was already available in the laboratory at the beginning of this PhD work and has therefore been described in detail previously. [Gah04, Lis05] However, an overview of the main components is given, including a description of the vacuum, laser and electronic setup.

3.2.1 UHV Components

The vacuum chamber is separated into two parts on top of each other, preparation and spectrometer chamber, which can be separated by a gate valve. A base pressure of $1 \cdot 10^{-10}$ and $8 \cdot 10^{-11}$ mbar in the preparation and the spectrometer chamber is achieved by a turbo molecular and an ion getter pump, respectively.[33] The arrangement of the UHV devices in the two chambers is given in Fig. 3.03. The preparation chamber consists of a sputter gun, an electron gun, a quadrupole mass spectrometer (QMS), a LEED spectrometer, a pinhole doser, and two

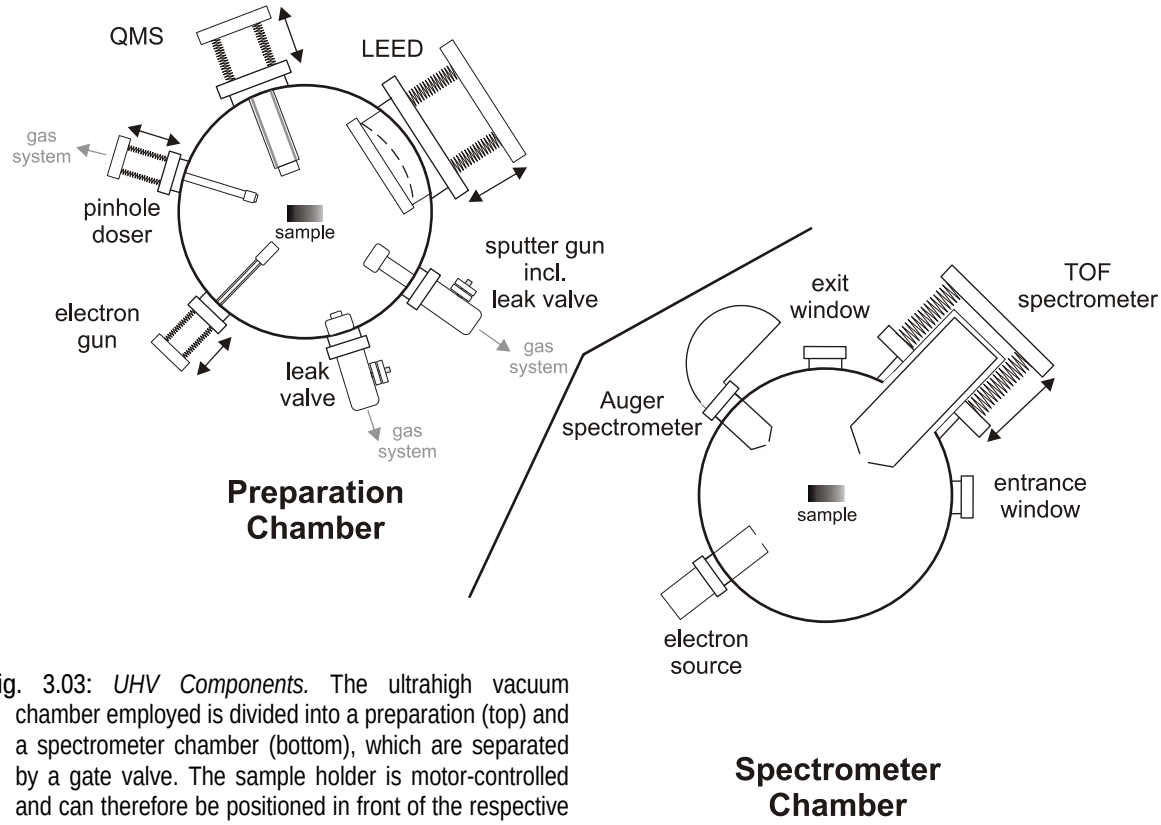

Fig. 3.03: *UHV Components.* The ultrahigh vacuum chamber employed is divided into a preparation (top) and a spectrometer chamber (bottom), which are separated by a gate valve. The sample holder is motor-controlled and can therefore be positioned in front of the respective instruments.

[33] The required fore-vacuum is reached by a membrane and a turbo drag pump.

leak valves.[34] In the spectrometer chamber the time of flight (TOF) and the Auger spectrometer are installed. The leak valves, sputter and electron gun are used to prepare the metal substrates (cf. 3.3) while QMS, LEED, and Auger spectrometers are employed to characterize the surfaces and the adsorbate layers, respectively. The pinhole doser enables the preparation of ice and ammonia layers without risking the good base pressure of the chamber.

The sample is connected to a stepper motor-controlled manipulator, which enables movements in the x, y, and z directions and a 360° rotation of the crystal to reach all installed UHV instruments. The sample holder (Fig. 3.04) is attached to a helium flow cryostat (F), which allows cooling of the crystals to ~30 K. The Ru(001) crystal (Ø 8 mm, 2 mm thick) and the Cu(111) crystal (Ø 9 mm, 3 mm thick) are mounted by 0.4 mm tantalum wires (B) to the sample holder, respectively.[35] The gold-plated copper legs (D) are isolated from the primary sample holder (E) by sapphire plates, but are electrically connected to copper wires (H), which allow resistive heating of the sample (see below). The temperature is measured by a NiCr/Ni thermocouple (G), which is spot-welded onto the side of the Ru(001) or inserted into a drill hole in the Cu(111) crystal, respectively.[36]

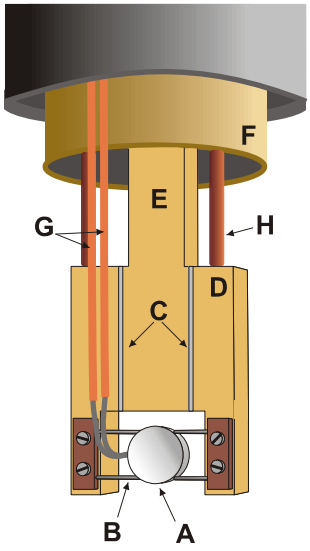

A) crystal
B) tantalum wires
C) sapphire plates
D) gold-plated copper legs
E) holder
F) cryostat
G) thermocouple
H) current connection

Fig. 3.04: *Sample Holder.* The sample is mounted via two tantalum wires on the gold-plated copper legs, which allow a current flow through the crystal. The holder is isolated from these electric contacts by sapphire plates and attached to the He cryostat.

The sample temperature can be adjusted by different procedures, depending on the respective application:

(i) By applying a voltage at the copper feed-throughs, a current flows through the copper legs, tantalum wires, and sample. Due to the high resistivity of the tantalum, the crystal is heated resistively; with currents up to 25 A the crystals may be heated up to 1000 K. Using a temperature controller, it is possible to keep the temperature constant within a range of 90 and 1000 K with an accuracy of 0.02 K. In addition, the controller allows a ramping of the temperature at 0.1 - 3.0 K/s.

As it is not possible to perform temperature dependent 2PPE measurements while heating the sample resistively, two relays are attached to the copper feed-throughs.

[34] In addition, the preparation chamber is connected to a magazine chamber which allows simple sample transfer under UHV. To attach new samples to the sample holder a screwdriver is installed in the preparation chamber.
[35] In fact, the sample holder consists of a fixed and a moveable part, which allows sample exchange under UHV. For simplification, these details are left out in Fig. 3.04.
[36] Due to its high electrical and heat conductivity, it is impossible to spot-weld on a copper crystal.

They disconnect the power supply from the sample during data acquisition and allow the required bias potential of the crystal to be set (cf. 3.2.3).

(ii) For the preparation of the Ru(001) crystal it is necessary to reach higher temperatures than 1000 K (cf. 3.3.1), which may be achieved by using the electron gun (Fig. 3.03). Its core is a commercial halogen lamp (50 W / 12 A) filament. The electrons are generated by applying 3 A to the filament and are accelerated onto the back side of the crystal by a positive potential <600 V. In principle it is possible to heat the sample up to 1600 K, but due to the rather low melting point of the NiCr/Ni thermocouple the maximum temperature used was 1540 K.

(iii) To perform temperature-dependent *and* time-resolved 2PPE measurements it is troublesome to use the above-described relays procedure, as it would multiply the data acquisition time considerably.[37] Therefore the embedded cryostat-heating was employed to carry out time- *and* temperature-dependent studies. However, this procedure also has disadvantages: Due to the slow response of sample temperature to heating and cooling of the cryostat, a constant, equilibrated sample temperature requires careful adjustment and therefore a certain amount of time as well. To maintain a good sample quality,[38] it is necessary to balance between temperature accuracy and data statistics. This trade-off was achieved by a temperature stability of ±0.5 K and approximately a third of the statistics achieved by minimum temperature 2PPE measurements.

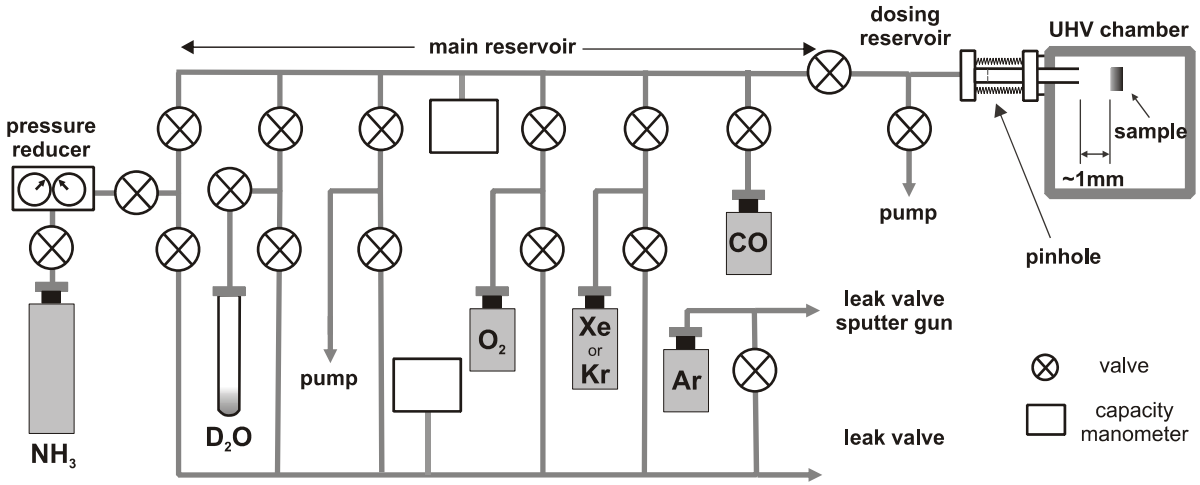

Fig. 3.05: *Gas System.* Besides the adsorbates, NH_3 and D_2O, several rare gases, oxygen, and carbon monoxide are connected to the gas system. To avoid contamination of the UHV, the water and ammonia pressure are dosed via the pinhole doser directly onto the sample with a negligible pressure rise in the chamber.

[37] Each of the 100-300 time steps of a time-resolved 2PPE experiment is measured 10-30 times. To keep the temperature constant, heating of the sample after every step would be required. As heating and switching takes ~2 s, this would at least triple the data acquisition time. For details on the data acquisition see subsection 3.2.3.

[38] Even under UHV rest gases slowly contaminate the adlayer; samples have to be refreshed after approximately 4-5 hours.

For sample preparation it is necessary to introduce several gases into the UHV chamber. Therefore, as depicted in Fig. 3.05, leak valves and a pinhole doser are connected to a gas system: Oxygen and carbon monoxide for the preparation and characterization of the Ru(001) crystal, argon gas used for sputtering of the samples (cf. 3.3.1), other rare gases for temperature calibration (cf. appendix C), and the adsorbates, D_2O and NH_3.

The gas system is divided into two sections, an upper and a lower part, so that reactive gases (e.g. D_2O and O_2) are not dosed via the same pipes on the same day or during the measurement period; to avoid contaminations and isotope exchange between the two employed adsorbates, the gas system is thoroughly baked out before switching from D_2O to NH_3 and vice versa. The main reservoir allows for the adjustment of the desired dosing pressure, and a connection to the pump system at the dosing reservoir facilitates a defined ending of the dosing time. A description of the preparation procedures is given in section 3.3.

3.2.2 Laser System

This work was done employing a commercial, tuneable femtosecond laser system from *Coherent*. Two diode-pumped continuous wave (cw) solid-state lasers (5 W and 10 W) pump the oscillator (Mira) and the regenerative amplifier (RegA). The RegA output can be coupled into two optical parametric amplifiers (OPA) working in the infrared (IR) and visible (VIS), respectively. The laser system has been used for several projects and has therefore been described previously. [Hot99, Gah04, Lis05] Thus, only a brief description of the setup and the underlying non-linear processes is given here.

A sketch of the optical setup is given in Fig. 3.06. The fs-laser pulses are generated in the Mira. Its laser medium is a titanium-doped sapphire (Ti:Sa) crystal, which exhibits a broad absorption spectrum (400 - 600 nm) around a maximum of 490 nm. The long-living excited states of the Ti:Sa are pumped by the 532 nm cw output of the Verdi V-5.[39] The broad emission spectrum of the Ti:Sa is centered at 800 nm. Ultrashort laser pulses are generated in the Mira cavity upon constructive interference of the longitudinal modes; the pulse duration is inverse proportional to the bandwidth of mode spectrum:

$$\frac{\lambda^2}{\Delta\lambda} = c \cdot \Delta t \qquad \text{(central wavelength } \lambda\text{, light velocity } c\text{)} \qquad (3.1)$$

Mode-locking is achieved by utilization of the intensity dependence of the refractive index of the Ti:Sa crystal

$$n(\omega, I) = n_0(\omega) + I \cdot n_2(\omega), \quad \text{(frequency } \omega\text{, intensity } I\text{)} \qquad (3.2)$$

which leads to the so-called Kerr-Lens Effect. [Rul98, Dem03] A spatially uneven intensity distribution leads, due to equation (3.2), to a spatial distribution of the refractive index. The less intense parts of a pulse in the time domain, the flanks, and remaining cw modes, are not

[39] The pump laser medium is a cooled $Nd:YVO_4$ crystal, which is pumped by two laser diodes at 808 nm. This output is frequency-doubled in a KDP (*potassium dihydrogen phosphate*, KH_2PO_4) crystal and coupled into the oscillator.

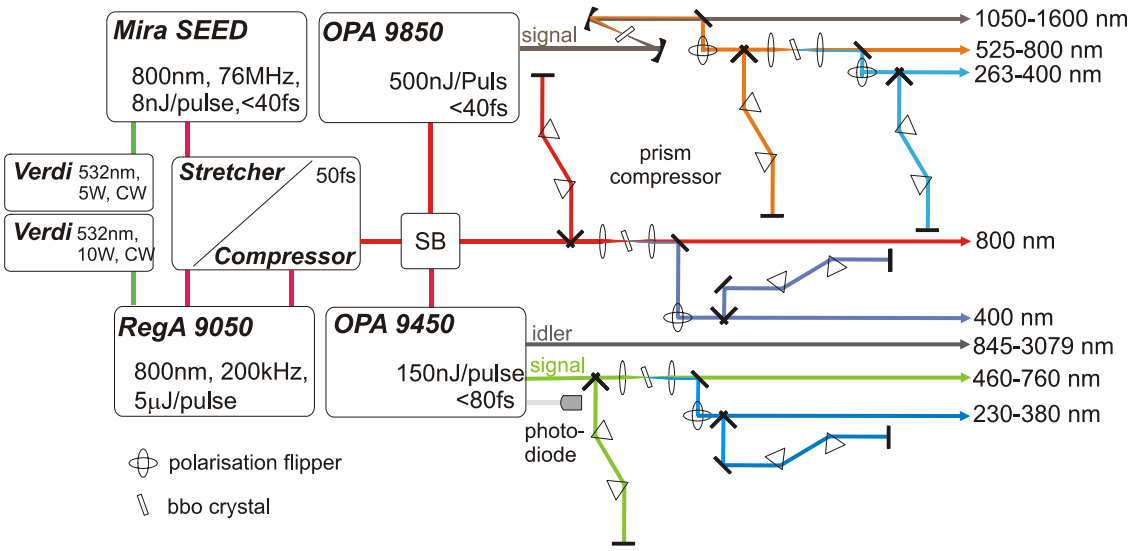

Fig. 3.06: *Laser System.* The oscillator output is stretched and compressed before and after regenerative amplification, respectively. In a switch box (SB) the RegA output can be coupled into two OPAs, which provide tuneable femtosecond laser pulses in the IR and VIS range. Prism compressors are used to account for temporal chirp; UV light is generated by frequency doubling in non-linear BBO crystals.

focused as much as the temporal maximum. Therefore, the laser medium acts like a lens, which allows the clipping of the weak intensity parts of the pulse by a slit in the cavity. The intensity fluctuations needed are achieved in the Mira by a moveable mirror that disturbs the beam in the resonator.

The Mira works at a repetition rate of 76 MHz and produces 8 nJ pulses of 40 - 50 fs duration. In principle, the oscillator can amplify bandwidths up to 100 nm, which would lead to a generation of pulses below 20 fs. On the other hand, a reduction of the bandwidth to 30 – 40 nm by a birefringent filter enables the variation of the Mira's central wavelength between 750 and 850 nm. As the RegA cannot amplify bandwidths higher than 30 nm in any case, the opportunity of tuneability was utilized.

The output pulse energies provided by the Mira are not sufficient to drive an OPA. To achieve the necessary photon density on the order of µJ per pulse, the Mira output is regeneratively amplified. To avoid damage of the laser-active medium in the RegA (also Ti:Sa) due to the high top intensities, the Mira output is stretched in the time domain (see Fig. 3.06). This is achieved by a temporal separation of the frequency components of the pulse; a so-called temporal chirp is introduced. By passing through four gratings the pulse is elongated to several nanoseconds. After the amplification, this expansion is reversed by the same procedure[40] and the pulses are compressed to ~50 fs.

The integral components of the RegA are – besides the Ti:Sa crystal – a quality ("Q-") switch, which hinders spontaneous lasing, and an opto-acoustic modulator, which is used as a cavity dumper. The population inversion in the laser medium is pumped by a Verdi V-10 laser.

[40] A concave mirror in the optical path of the stretcher is leads to an effective negative path length.

During this population increase the Q-switch reduces the performance of the cavity. As soon as the inversion population reaches its maximum the cavity dumper couples one Mira pulse into the resonator, and the Q-switch optimizes the cavity. While running through the resonator, the pulse reduces the inversion and reaches its maximum intensity after 20 – 30 round trips. Finally, the Q-switch reduces the cavity quality again, so that an anew population inversion can be established. The intensity distribution of the RegA output beam as a function of time and wavelength is depicted in Fig. 3.07. It was taken after recompression using a Grenouille (*Swamp Optics*), which also allows characterization of the spatial beam profile (not shown).

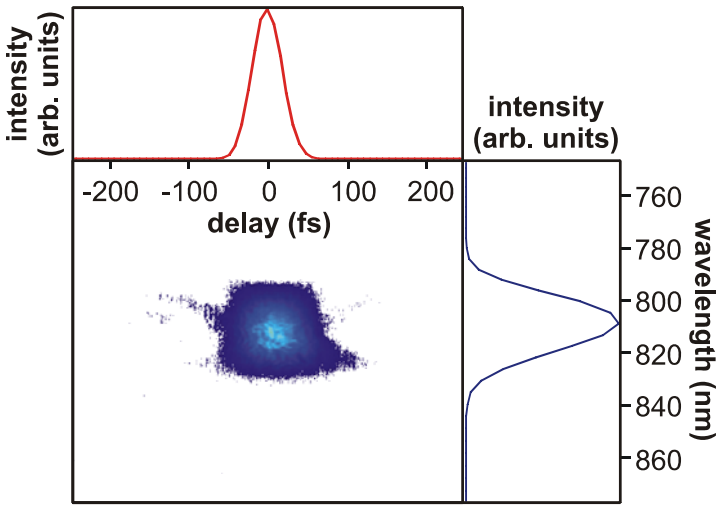

Fig. 3.07: *Pulse Characterization of the Compressed RegA Output.* The intensity distribution of the pulses is a Gaussian in the time and wavelength domain.

Most experiments require different photon energies than the ~1.5 eV provided by the RegA. For this purpose two optical parametric amplifiers are integrated in the employed setup. They take advantage of the non-linearity of the dielectric susceptibility, which enables optical mixing techniques like second harmonic generation (SHG) or difference frequency generation (DFG). When the electric field of the incoming light becomes comparable with the local fields in a crystal, higher order terms in the macroscopic polarization become important:

$$\vec{P}(t) = \varepsilon_0 \chi^{(1)} \vec{E}(t) + \varepsilon_0 \chi^{(2)} \vec{E}^2(t) + \varepsilon_0 \chi^{(3)} \vec{E}^3(t) + \ldots \tag{3.3}$$

$\chi^{(n)}$ is the susceptibility of n^{th} order, described by a tensor of rank $(n+1)$, which depends on the symmetry of the non-linear medium.[41] If light of different frequencies ω_1 and ω_2 passes through the crystal, oscillating atomics dipole moments are induced, which are themselves microscopic sources of the frequencies ω_1 and ω_2. The quadratic term in (3.3) also leads to contributions in the polarization of the doubled frequencies, their difference, and sum. A macroscopically relevant light wave can be formed only if the phase matching condition

$$\vec{k}(\omega_1 \pm \omega_2) = \vec{k}(\omega_1) \pm \vec{k}(\omega_2) \tag{3.4}$$

is fulfilled (momentum conservation). The maximum efficiency of this process is reached if all three beams propagate collinearly through the medium. With the phase velocity

[41] It can be understood as a measure of the restoring force initiated by the high fields affecting the electron shells in the crystal.

$$v_{ph} = \frac{\omega}{k} = \frac{c}{n(\omega)}, \tag{3.5}$$

where $n(\omega)$ is the refractive index, equation 3.4 becomes equivalent with

$$n_1 = n_2 = n_3 \quad \text{with} \quad n_i = n(\omega_i),\ i = 1, 2, 3 \quad \text{and} \quad \omega_3 = \omega_1 \pm \omega_2 . \tag{3.6}$$

In uniaxial birefringent crystals this phase matching condition is fulfilled if two of the light waves are ordinary waves, i.e. their polarization is in the *x*-*y*-plane perpendicular to the optical axis of the medium, and one is an extraordinary wave (polarized in the plane spanned by the optical axis and the incident beam).[42]

The phase matching can be achieved by varying the angle of incidence. In the OPAs employed here, β-barium borate (BBO) crystals are used to perform DFG. Their thickness is adjusted to the contributing wavelengths. The incident RegA output is separated by a beam splitter to provide 75% of the power as the *pump* and 25% as the *seed* of the DFG process: Collimation of the seed beam into a sapphire plate produces, due to self phase modulation, a wide white light continuum ranging from IR to UV. [43] This spectrum is responsible for the tuneablity of the OPA, as it provides a wide range of frequencies ω_2 for the DFG. In the case of the IR-OPA the seed beam remains at 800nm, while it is frequency-doubled in the VIS-OPA in a BBO to provide the correct ω_1 for DFG in the visible range. Pump and seed beam are spatially and temporally overlapped in another BBO crystal. Because the pump is strongly chirped in time and space, not only the phase matching angle must be changed for tuning the amplifier to a different output wavelength, but also the overlap has to be readjusted. To achieve high efficiency, each pulse passes through the DFG crystal twice. As two frequencies result in DFG (ω_2 and ω_1-ω_2), the OPAs have in principle two output signals: *Signal* and *idler*. In the case of the IR-OPA both are in the infrared (1100 – 1600 nm and 1600 – 2900 nm); the VIS-OPA provides signal pulses between 460 and 760 nm and an idler in the infrared (845 – 3080 nm).[44]

The OPA signal and the RegA output can be frequency-doubled by further BBO crystals in the optical paths (see Fig. 3.06), so that photon energies in the UV range are accessible for 2PPE spectroscopy. In all VIS and UV beam paths, prism compressors are inserted in order to decrease the pulse duration.

Fig. 3.08 shows the optical setup in front of the UHV chamber. A delay stage in the optical path of the UV allows for the time-resolved 2PPE spectroscopy: The time delay for the pump-probe experiment is achieved by varying the path length. The beams are coupled into the UHV

[42] In the case of SHG in β-barium borate (BBO) crystals (see below) this leads to a flip of polarization from p to s. To account for this effect, polarization flippers are inserted in the beam path behind every BBO (cf. Fig. 3.06).
[43] A small fraction of the white light is sent to a photodiode (see Fig. 3.06) that provides the start pulse for the time of flight measurement (cf. 3.2.3).
[44] The phase-matched part of the white light spectrum determines the spectral width and hence the duration of the output pulses. Due to a broader phase matching region and the smaller dispersion in the IR are the output pulses shorter (< 40 fs) than the ones of the VIS-OPA (< 80 fs).

chamber collinearly and focused onto the sample. Using flip mirrors the beams may be sent to a fast photodiode that is used to define zero time delay within a time window of ~50 ps (1.5 cm). In this way it is assured that the difference in the optical path lengths of both colors is within the range of the delay stage (11.5 cm) so that the temporal overlap of the pulses can be found. The accurate time zero determination is done on the sample by scanning the stage and observing the photoelectron intensity. The 2PPE intensity increases significantly due to the correlated signal of pump and probe pulse when the temporal overlap is established. The spatial overlap of the two beams is achieved by the aid of a pinhole in front of the UHV chamber. In addition, the spot profiles can be analyzed by a CCD (charged-coupled device) camera.

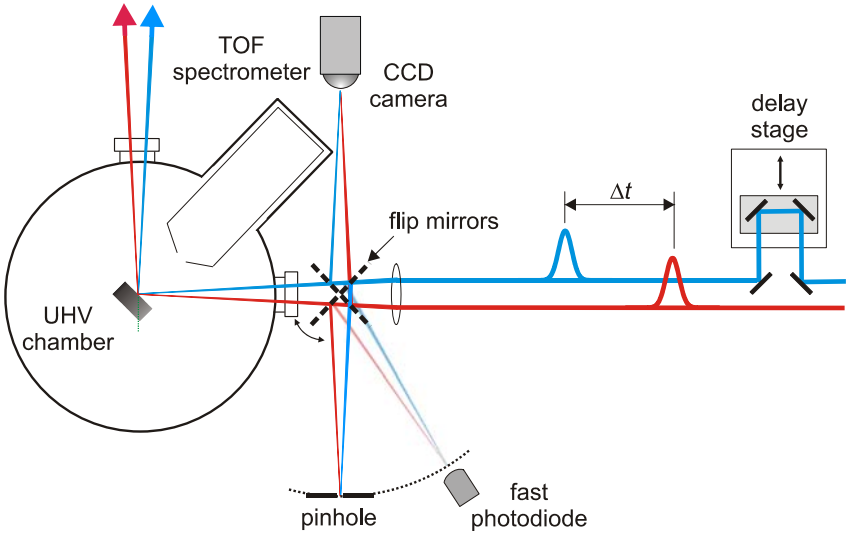

Fig. 3.08: *Experimental Setup.* Before coupling the beams into the UHV chamber the UV light passes a delay stage that varies the optical path length. A photodiode is used for time zero determination, and a pinhole to achieve spatial overlap. Using the CCD camera the spot profile is characterized.

3.2.3 Time of Flight Detection and Signal Processing

The kinetic energy determination of the photoelectrons was done using a linear time of flight spectrometer combined with several devices for the signal processing. This part of the experiment has been described in detail previously. [Kno97b, Hot99, Gah04, Lis05] Briefly, the main part of the TOF spectrometer is a grounded, field-free flight tube of 297 mm. At one end it is conical and has an entrance hole (Ø 1.5 mm) for the photoelectrons; the electron detector is installed at the other end. The irradiated spot on the sample is positioned 3 mm in front of the entrance, which can be adjusted using a CCD camera. Therefore, the photoelectrons travel L = 30 cm before being detected. The flight tube, including the entrance cone, it is coated with a graphite layer (work function Φ_{TOF} = 4.45 eV) in order to ensure a constant and homogeneous work function. Due to the mentioned geometrical conditions, the spectrometer has an acceptance angle for photoelectrons of ±3.8°. The spectrometer is surrounded by a μ-metal envelope, which shields the flight tube from magnetic fields. This cladding has small holes to enable the entrance and exit of the laser beams. They illuminate the sample at 45° so that the electrons are detected at normal emission. It is also possible to rotate the sample (10°...-16°) in order to perform angular-resolved experiments.

The core of the detector consists of a pair of micro channel plates (MCP). After drifting 300 mm through the flight tube, the electrons pass through a graphite-coated grid that screens the flight tube from the 300 V that accelerate the electrons onto the MCPs. The incoming electrons initiate electron cascades, which are coupled out of the UHV by a condensator. The resulting voltage pulse is used as the *stop*-pulse for the TOF determination.

The photodiode behind the VIS-OPA (Fig. 3.06) provides the *start*-pulse. Both signals pass through discriminators, which smooth out fluctuations and produce negative pulses (see Fig. 3.09).[45] These signals are sent to a *time-to-digital* card in the computer, which allows a time difference detection with an accuracy of 0.25 ns without dead time between the events. Its multi-hit capability leads to the high maximum count rate of 10^6 cts/s.

The computer is also equipped with a multi-function measurement card that has eight differential A/D- and two D/A-converters (12 bit, 10^6 s^{-1} max. sampling rate), two 24 bit counters, eight logical, and ten programmable channels. The measurement software has been programmed in a *LabView* environment previously.

For time of flight measurements the detected events are sorted into 8192 bins according to their respective TOF. For the time-resolved measurements the delay stage in the optical beam path is controlled via a GPIB port. For temperature dependent 2PPE spectroscopy two relays, which are attached to the copper feed-throughs (cf. 3.2.1), are controlled via the PC. The sample temperature is adjusted using an external temperature controller.

Generally, during a time-resolved 2PPE measurement, each time step (each delay stage position) is maintained for 800 ms of data acquisition time (DAQ). The data is acquired for the entire delay range of interest. To ensure sufficient statistics, these scans are repeated 10 to 30

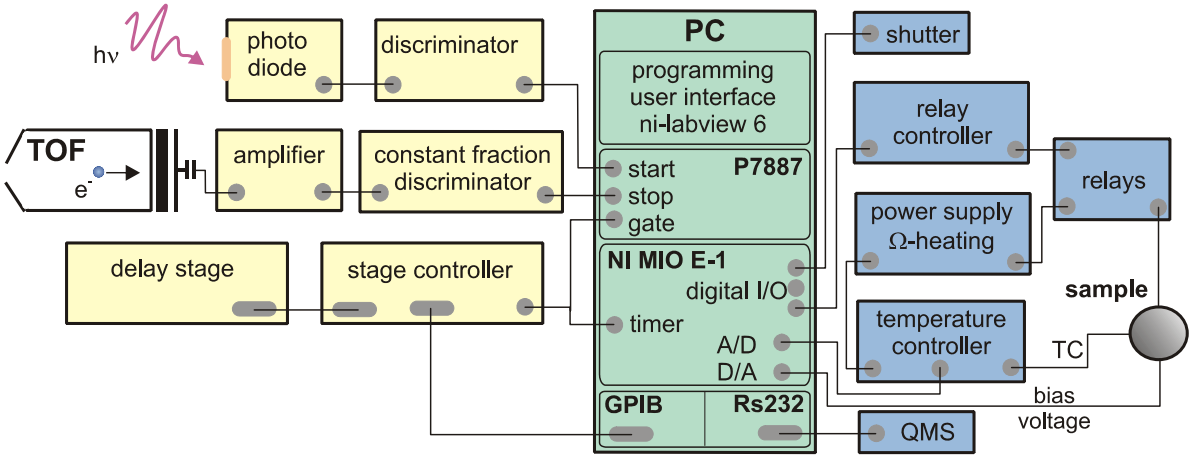

Fig. 3.09: *Signal Processing.* TOF measurement (yellow) and temperature control (blue) are performed by a PC using a *LabView* environment. See text for details.

[45] The *start*-pulses are very stable, so that an ordinary discriminator is sufficient. The stop pulses in contrast have strongly varying amplitudes so that a constant fraction discriminator is required. It always triggers, regardless of the pulse height, the same relative position of the rising edge of the signal.

times. This procedure reduces the risk of long-term changes like sample corrugations or laser intensity variations being reflected in the data. However, the measurement time is increased due to the repeated dead-time during delay stage movement.

TOF to Kinetic Energy Conversion: To make 2PPE measurements possible on samples with lower work functions than the TOF spectrometer (4.45 eV), it is possible to apply a bias voltage between sample and flight tube. The latter remains grounded to enable a field-free drift of the electrons. Neglecting the short acceleration path length, the kinetic energy of a photoelectron after emission is

$$E_{kin} = \frac{1}{2} m_e \left(\frac{L}{t} \right)^2 - eU \,. \tag{3.7}$$

Here, L is the distance between sample and detector and eU is the sum of the potential differences according to

$$eU = \Phi_{sample} - \Phi_{TOF} + eU_{bias} \,. \tag{3.8}$$

As shown in Fig. 3.10, it is necessary to apply a bias voltage that is sufficient to cancel out the work function difference between sample and spectrometer, so that even the slowest photoelectrons are detected.

The real TOF of the photoelectrons differs, of course, from the measured time difference between *start*- and *stop*-pulse. The measured time t_m differs from the real flight time t by a constant value t_0, the time that the *start*-signal propagates through the electronics. As the kinetic energy depends quadratically on the flight time, but linearly on the applied bias voltage, t_0 can be determined by a series of spectra at different voltages:

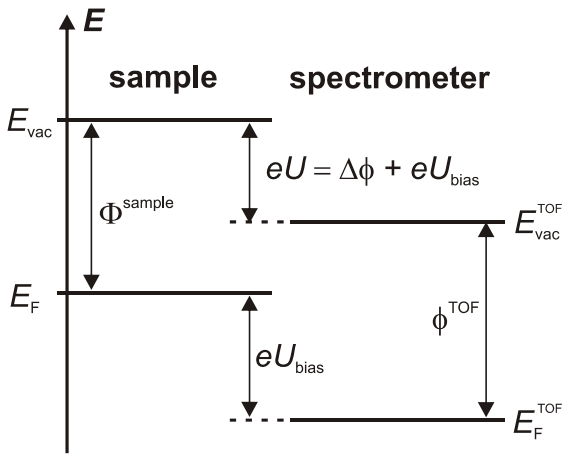

Fig. 3.10: *Potential Diagram of Spectrometer and Sample.*

$$E_{kin} = \frac{1}{2} m_e \left(\frac{L}{t_m - t_0} \right)^2 - \Phi_{sample} + \Phi_{TOF} - eU_{bias} \tag{3.9}$$

As the relation between TOF and kinetic energy is non-linear, the intensities also have to be rescaled:

$$\frac{\mathrm{d}N}{\mathrm{d}E_{kin}} = \frac{\mathrm{d}N}{\mathrm{d}t} \cdot \left| \frac{\mathrm{d}t}{\mathrm{d}E_{kin}} \right| = \frac{\mathrm{d}N}{\mathrm{d}t} \cdot \frac{(t_m - t_0)^3}{m_e \cdot L^2} = \frac{\mathrm{d}N}{\mathrm{d}t} \cdot \sqrt{\frac{m_e \cdot L^2}{8}} \cdot E_{kin}^{-3/2} \tag{3.10}$$

The bins related to low energies are stretched according to (3.9) and weighted more heavily due to (3.10); for the high energy bins vice versa.

The rotatable sample provides the opportunity to perform angle-resolved measurements. Because the momentum of the photons is negligible, information about the momentum of the electrons parallel to the sample surface, $\hbar k_{\parallel}$, is accessible. As the Cu(111) surface is translationally symmetric, $k_{\parallel}$ is conserved and a good quantum number. [Hot99] Unless mentioned otherwise, the presented measurement were all done at $k_{\parallel}=0$, i.e. at normal emission. However, if the sample is rotated by an angle φ, the electron momentum is determined by

$$k_{\parallel}(\varphi, E_{kin}) = \sin\varphi \cdot \sqrt{\frac{2m_e}{\hbar^2} E_{kin}}\ .^{46} \tag{3.11}$$

[46] Angle-resolved 2PPE measurements of the amorphous NH_3/Cu(111) interface are presented in appendix A.

3.3 Sample Preparation and Characterization

Accurate preparation of the samples investigated is of crucial importance, as the spectral features of bare and adsorbate-covered metal surfaces are very sensitive to contaminations. Therefore, it is necessary to accurately prepare both, metal surfaces and the adsorbate layers. The preparation of the substrates was done following standard procedures. Thermal desorption spectroscopy (TDS) was employed to characterize the ice and ammonia layers.

3.3.1 Metal Substrates

The Cu(111) surface was routinely (daily) subjected to cycles of Ar^+ sputtering and annealing. Sputtering is known to ablate contaminations from metal surfaces. Using an argon background pressure of ~$2 \cdot 10^{-6}$ mbar the rare gas atoms were ionized at the filament of the sputter gun and accelerated onto the crystal with a high voltage of 700 V for five minutes.[47] The subsequent annealing of the sample to 700 K for 20 min then leads to a smoothening of the crystal surface. Initially, this procedure was repeated twenty times with the new Cu(111) crystal to assure good sample quality. The periodicity of the surface lattice was checked by LEED measurements and 2PPE spectra: The Cu(111) surface state and the crystals work function are highly sensitive to contaminations.

The highly reactive Ru(001) surface had to undergo a longer preparation procedure. After sputtering with 0.8 - 1.0 V, the sample was annealed ("roasted") in an oxygen background pressure of $1 \cdot 10^{-7}$ mbar. Due to the high melting point of ruthenium this could be done at 1450 K.[48] Carbon contaminations of the crystal, which are typical for ruthenium surfaces, react with the present oxygen during the "roasting", forming carbon monoxide, which desorbs at temperatures below 600 K. After 20 min the oxygen supply is stopped and the temperature increased to 1510 K to ensure a smooth surface. Finally, to get rid of any remaining oxygen, the sample is heated to 1540 K for 20 s. As in the case of the Cu(111) crystal, the sample quality was checked with LEED. In addition Auger electron spectra and CO thermal desorption (TD) spectra were taken to confirm a contamination-free surface.[49]

[47] The ion current was ~1.5 μA.
[48] These high temperatures were reached by usage of the electron gun (see 3.2.1).
[49] TD spectra of CO/Ru(001) are very sensitive to oxygen contamination of the surface (see [Pfn83, Kos92]).

3.3.2 Adsorbate Layers

The ice and ammonia layers are prepared using the pinhole doser. The main reservoir of the upper gas system (cf. Fig. 3.05) is filled with the desired adsorbate gas at a pressure of 0.5 and 0.2 mbar for D_2O and NH_3, respectively. After positioning the sample in front of the doser, the gas is introduced into the dosing reservoir. This expansion leads to a pressure decrease to 0.28 and 0.13 mbar, respectively. Due to the small pinhole this pressure remains stable during dosing. Fig. 3.11 shows the background pressure evolution of NH_3 ($m = 17$ amu) in the chamber during the dosing procedure. After the designated exposure time has elapsed, the pump valve (Fig. 3.05) is opened. The pumping of the dosing reservoir is accompanied by a sudden background pressure drop, as for example after 120 s indicated by "A" in Fig. 3.11. The sample is then driven away from the pinhole doser at "B". This leads to an increase of the NH_3 background signal.

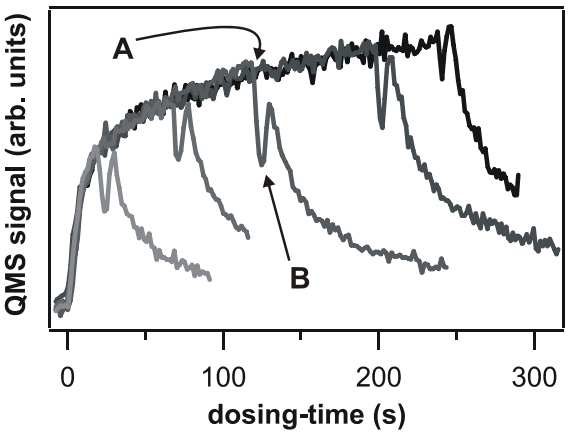

Fig. 3.11: *Background Pressure During NH_3 Dosage.* The end of ammonia exposure is defined by the opening of the pump valve (A). The sample is driven away from the doser at B.

The absolute coverage of the adsorbate layers is determined employing thermal desorption spectroscopy. To do so, the sample was driven in front of the quadrupole mass spectrometer. Using resistive heating and the temperature controller, the crystal was heated with a constant heat ramp of 0.25 K/s (D_2O) and 2.2 K/s (NH_3).[50]

Ice on Metal Surfaces: The D_2O employed in this work has an isotope purity of 99.9 % (*Sigma Aldrich*). To ensure cleanness, *freeze-pump-thaw* cycles are performed: The deuterated water is frozen with liquid nitrogen in the test tube plugged to the gas system. During the melting the vapor is pumped away, so that contamination with more volatile gases (as O_2) can be excluded. This procedure was repeated several times before the first 2PPE measurements.

Fig. 3.12 (top) shows TD spectra of various coverages of D_2O/Ru(001) dosed at 90 K.[51] The QMS signal (m = 20 amu) is plotted as a function of sample temperature.[52] The spectra exhibit three features: (i) The multilayer peak, (ii) the bilayer peak, and (iii) a high-temperature signal around 200 K (inset).

[50] The detection efficiency for NH_3 is much smaller than for D_2O. This was compensated by a faster ramping of the temperature.

[51] These spectra were taken in the framework of my diploma thesis and C. Gahl's PhD work [Gah04].

[52] The standard calibration of the NiCr/Ni thermocouple leads to strong deviations of the desorption temperatures of rare gases adsorbed on the employed metal surfaces. Therefore the temperature was recalibrated according to the literature values for Ar, Xe, and Kr desorption. See appendix C for details.

(i) The zero-order multilayer desorption kinetics are apparent by the coverage-independent onset of desorption at ~150 K for all coverages and the peak maximum that shifts to higher temperatures with increasing total coverage. Ice layers adsorbed at 90 K are amorphous (cf. 2.4.1). The crystallization of these layers occurs at ~160 K and causes the kink in the TD spectra at this temperature:[53] As amorphous ice exhibits a higher vapor pressure than crystalline ice, [Smi96] the desorption yield is reduced upon crystallization, which results in the shoulder at 160 K. For the preparation of crystalline multilayers the D_2O is adsorbed at 157 K. As TD spectra of these coverages still exhibit a slight crystallization shoulder, the sample was afterwards annealed to 164 K to ensure full crystallization.[54]

(ii) The D_2O-Ru interaction is significantly stronger than the ice-ice interaction. Therefore the desorption of the first bilayer of D_2O/Ru(001) occurs at significantly higher temperatures than the multilayer desorption. The BL-peak saturates with increasing coverage and is finally superposed by the growing multilayer signal. The position of the bilayer peak maximum at 178 K is in agreement with literature. [Hel95a]

The absolute D_2O coverage is determined using the bilayer desorption yield as a mass equivalent. The integral of the 1.1 BL coverage is shown in the bottom panel of Fig. 3.12. It exhibits a kink at 157 K due to the decrease of D_2O desorption yield between multilayer and bilayer desorption, which is used to define the mass equivalent of 1.0(1) BL.

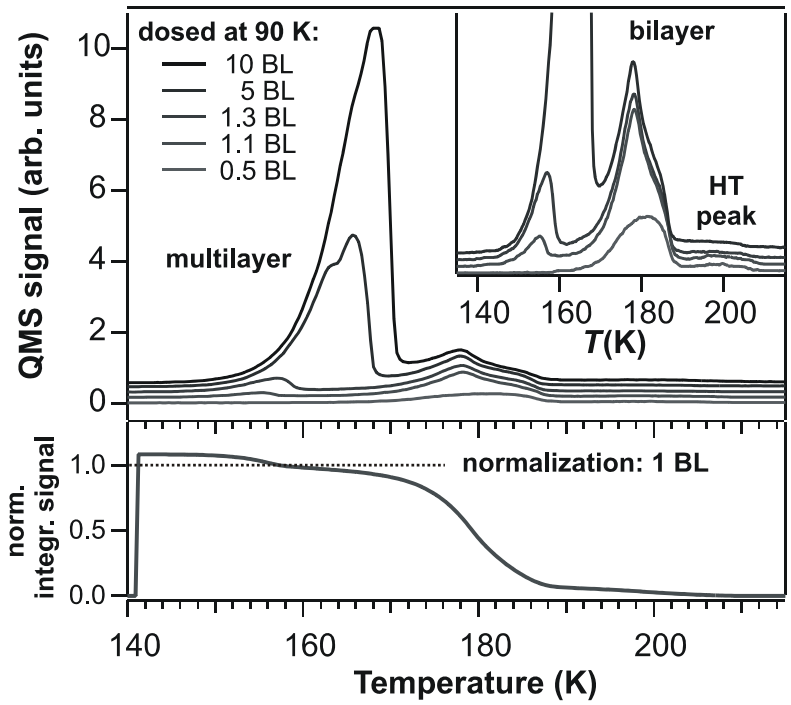

Fig. 3.12: *TD Spectra of D_2O/Ru(001).* Top: Thermal desorption spectra of several coverages of D_2O on the Ru(001) surface. The multilayer desorption peak exhibits at ~160 K a shoulder due to crystallization. The high-temperature (HT) peak probably results from dissociated ice on the Ru(001) surface (inset). Bottom: Integrated QMS signal for the 1.1 BL coverage. The signal is normalized to the kink previous to bilayer desorption. This value is used as a mass equivalent for the absolute D_2O coverage. (See text for details.)

[53] Actually the crystallization is a thermally activated process. Therefore the position of the kink in the TD spectra depends on the employed heating rate and adsorbate coverage.
[54] A detailed description of this procedure is given in [Gah04].

(iii) The height of the high-temperature (HT) peak (inset) is a measure for the quality of the ice layers: It was shown recently that bombardment of ice layers with low-energy electrons [Far05] and small contaminations of oxygen lead to a dissociation of the first bilayer of D_2O on Ru(001) (cf. 2.4.3). The dissociated water is more strongly bound to the substrate and therefore desorbs after recombination molecularly at higher temperatures. In the present work, the D_2O was purified with the above-mentioned *freeze-pump-thaw* cycles so that the HT-signal was well below 10% of the bilayer peak amplitude.

The ice-metal interaction for D_2O on Cu(111) is comparable to the ice-ice interaction. Therefore, no separated bilayer peak is observed in the TD spectra of D_2O/Cu(111). The determination of the absolute coverage was done by calibration of dosing time and pressure with the D_2O/Ru(001) data.[55] In addition the strong coverage dependence of the sample work function [Gah04] was used to cross-check the layer thickness.

NH_3/Cu(111): Thermal desorption spectra of ammonia on Cu(111) are shown in Fig. 3.13. They exhibit more substructures than the TDS of D_2O/Ru(001). Following the nomenclature of [Ben83], who investigated NH_3/Ru(001), the two high-temperature features are termed α_1 and α_2 and assigned to the first monolayer. Between 100 K and 120 K the second monolayer, β, desorbs, and at even lower temperatures a multilayer peak, γ, with zero-order desorption kinetics appears.[56] The integral of α_1 and α_2 is – as in the ice/metal case – used as a mass equivalent for the NH_3 coverage and is normalized to 1.0(2) ML (monolayer).[57]

As in the case of D_2O, a kink is observed in the TD spectra of NH_3/Cu(111). Here, it occurs at 100 K (indicated by the arrow in Fig. 3.13). Apparently, a structural rearrangement occurs upon heating to 100 K: The ammonia molecules are more strongly bound in the new configuration, than they were in the as-dosed structure. The vapor pressure accordingly decreases upon the transition. In agreement with present understanding [Ben83] the as-dosed layers are assigned to be amorphous. Accordingly, as NH_3 exhibits a crystalline phase below 200 K (cf. 2.4.1), the structural transition is assigned to the crystallization of the ammonia adlayers. This primary observation of an amorphous-crystalline transition of NH_3 under UHV conditions has considerable impact on the electron solvation and transfer dynamics at the NH_3/Cu(111) interface, as shown in chapter 5.

After the introduction of the employed technique, experimental setup, and sample preparation, the next section gives an overview of the 2PPE data analysis in this work. Here, the electron dynamics at ice- and ammonia-metal interfaces are studied time- and energy-

[55] The sticking coefficient of D_2O on Cu(111) *and* Ru(001) is unity for $T < 100$ K.

[56] In their work on NH_3 layers on Cu(111) Hertel et al. assigned the *sum* of β, α_1, and α_2 to the desorption of the *first* monolayer of ammonia. This work refrains from doing so, as (i) this nomenclature conflicts with the results of the NH_3/Ru(001) work in [Ben83], where a similar desorption structure was found, and (ii) the integral of α_1 and α_2 equals the integral of β.

[57] The larger error of 20% in the case of ammonia coverage determination results from the small temperature difference between α_1, α_2, β, and γ desorption. However, the error bar for relative coverage *differences* is with 5% much smaller.

resolved. Hence, paragraph 3.4.1 introduces the energy axis determination of the photoelectron spectra and 3.4.2 presents the analysis of the femtosecond population dynamics.

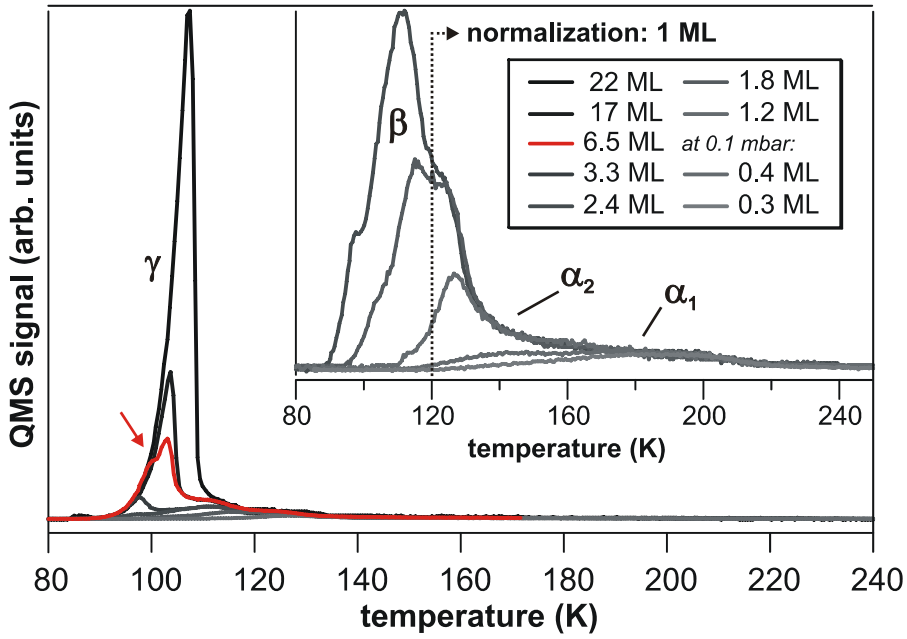

Fig. 3.13: *TD Spectra of NH_3/Cu(111).* The α_1 and α_2 feature correspond to desorption of the first monolayer, which is used as a mass equivalent for coverage determination. β is the second mono-layer, and γ arises from the multilayer desorption. The transition from amorphous to crystalline ammonia is apparent by the kink in the multilayer desorption peak at 100 K.

3.4 Data Analysis

Time-resolved two-photon photoelectron spectroscopy allows for the investigation of electron dynamics at adsorbate-metal interfaces in the time and energy domain. A typical time-resolved 2PPE spectrum of the bare Ru(001) surface is given in Fig. 3.14.[58] The main panel shows the 2PPE intensity in false color representation as a function of time delay between pump and probe pulse (bottom axis), intermediate state energy for negative delays (left axis) and binding energy for positive delays (right axis). As depicted in the top panel, positive delays correspond to electronic features excited by UV laser pulses; negative delays describe the inverted pulse sequence, where electronic states closer to E_F are populated.

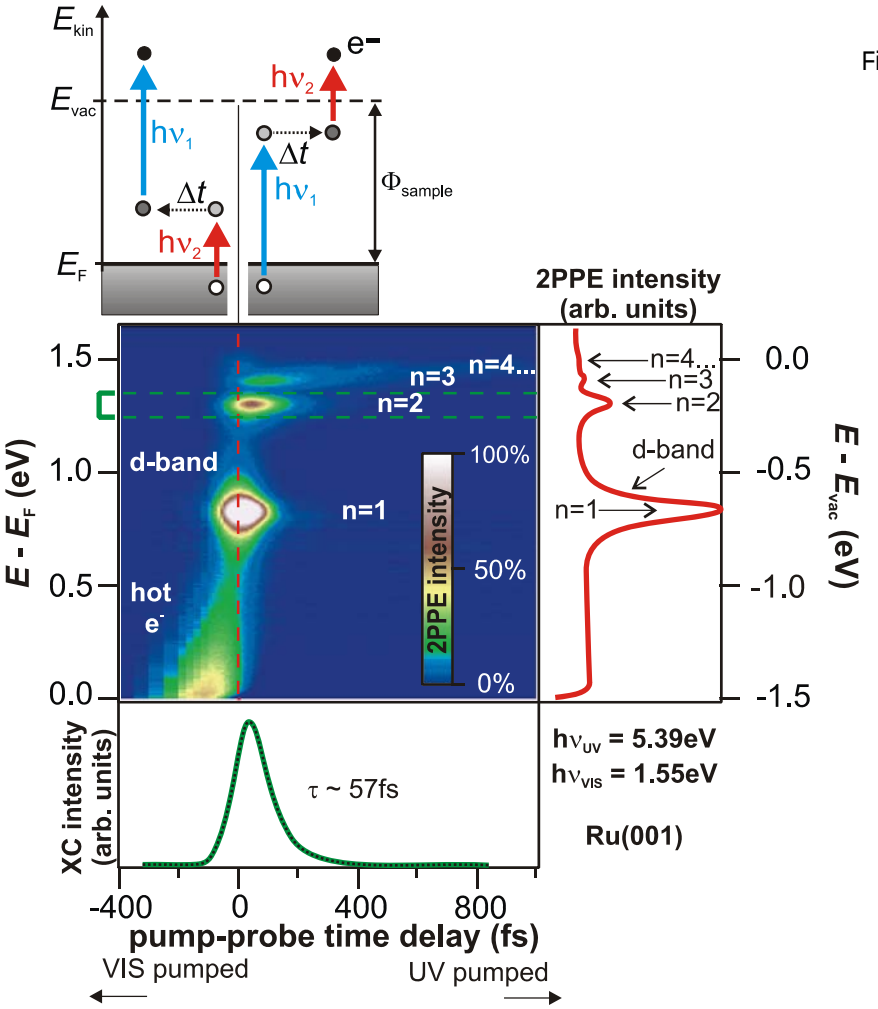

Fig. 3.14: *Time-Resolved 2PPE Measurement of the Bare Ru(001) Surface.* Main panel: 2PPE intensity in false color representation versus intermediate state energy with respect to E_F (left axis) and pump-probe time delay (bottom axis). Top: The pulse sequence is UV-VIS and VIS-UV for positive and negative time delays, respectively. Bottom: Integrated 2PPE intensity of the n = 2 image potential state (green line) in the energy interval indicated by the green dashed line in the main panel. The black dotted curve is a single exponential fit to the data leading to the indicated decay time. Right: Vertical cut through the 2D plot at t = 0 fs showing the intensity distribution of the observed spectral features: IPS series, d-bands, and hot electrons. The right axis denotes the binding energy of the image potential states.

[58] This measurement was done in the framework of my diploma thesis [Stä04] and C. Gahl's PhD work. [Gah04]

The two-dimensional representation ("2D plot") shows all spectral signatures of the Ru(001) surface between the Fermi Level E_F and vacuum level E_{vac}: The image potential state series, the unoccupied d-bands of Ru(001), and the hot electron dynamics. As indicated by their finite lifetime to positive time delays, the IPS are excited by UV photons and probed by visible light. They occur in a Rydberg-like series below the vacuum level (right axis) as discussed in subsection 2.4.2. The d-bands lie almost 1 eV above the Fermi Level[59] and are excited by VIS light. The hot electrons exhibit a finite lifetime to negative delays. Excited by visible photons they decay by inelastic scattering processes down to the Fermi Level. For details on their thermalization dynamics see references [Lis04, Lis05].

The two-dimensional 2PPE data sets (intensity as a function of time and energy) are quantitatively analyzed separately in the time and energy domain. For the analysis of the population dynamics the 2PPE intensity is integrated in the desired energy interval and plotted as a function of time delay. The bottom panel of Fig. 3.14 shows one exemplary cross-correlation (XC) trace obtained by integrating over the $n = 2$ IPS (dashed green lines in the main panel). Paragraph 3.4.2 gives a detailed description of this analysis. Information about the energetic positions of spectral features is achieved by the analysis of vertical cuts through the 2D plot at desired time delays. An exemplary 2PPE spectrum taken at $t = 0$ fs is depicted in the right panel of Fig. 3.14. Depending on the character of the electronic states, the data may be plotted versus different energy axes: Initial state, intermediate state, final state, or binding energy. The origin of these energy axes and the selection rules are the subject of the following paragraph.

3.4.1 Photoelectron Spectra

Paragraph 3.2.3 dealt with the determination of the kinetic energy E_{kin} of the photoelectrons from the TOF measurement. Equation (3.9) showed that the measured kinetic energy is composed of the "real" kinetic energy of the photoelectrons $\tilde{E}_{kin}$, the potential difference due to the sample and spectrometer work functions, and the applied bias voltage.

$$E_{kin} = \tilde{E}_{kin} + \Delta\Phi - eU_{bias} \quad \text{with} \quad \Delta\Phi = \Phi_{TOF} - \Phi_{sample} \tag{3.12}$$

To extract the "real" kinetic energy of the electrons this approach would require knowing the exact values of the involved work functions, which is – especially for new, not yet investigated systems – not necessarily the case. However, there is an alternative for the determination of photoelectron energy, since the samples leave well-defined fingerprints in the 2PPE spectra. The procedure for the energy determination is illustrated by Fig. 3.15. The upper panel shows a 2PPE spectrum of a multilayer coverage of amorphous D_2O/Ru(001) as a function of the measured kinetic energy according to (3.12). The mentioned fingerprints are the *secondary edge* and the *Fermi edge* and indicated by the arrows. The former is due to electrons that

[59] Actually, the spectral signature results from a surface resonance of the unoccupied bulk d-bands as discussed in 2.4.2. For simplification, this resonance is termed "d-band" in the following.

just overcome the sample's work function after absorption of the two photons, $h\nu_1$ and $h\nu_2$.[60] Their "real" kinetic energy is therefore zero. Shifting the energy axis, so that the secondary edge lies at 0 eV, therefore yields the "real" kinetic energy of the photoelectrons (Fig. 3.15, center). The "real" kinetic energy of the electrons results from:

$$\tilde{E}_{kin} = E_{kin} - E_{kin}(\text{Secondary Edge}) \tag{3.13}$$

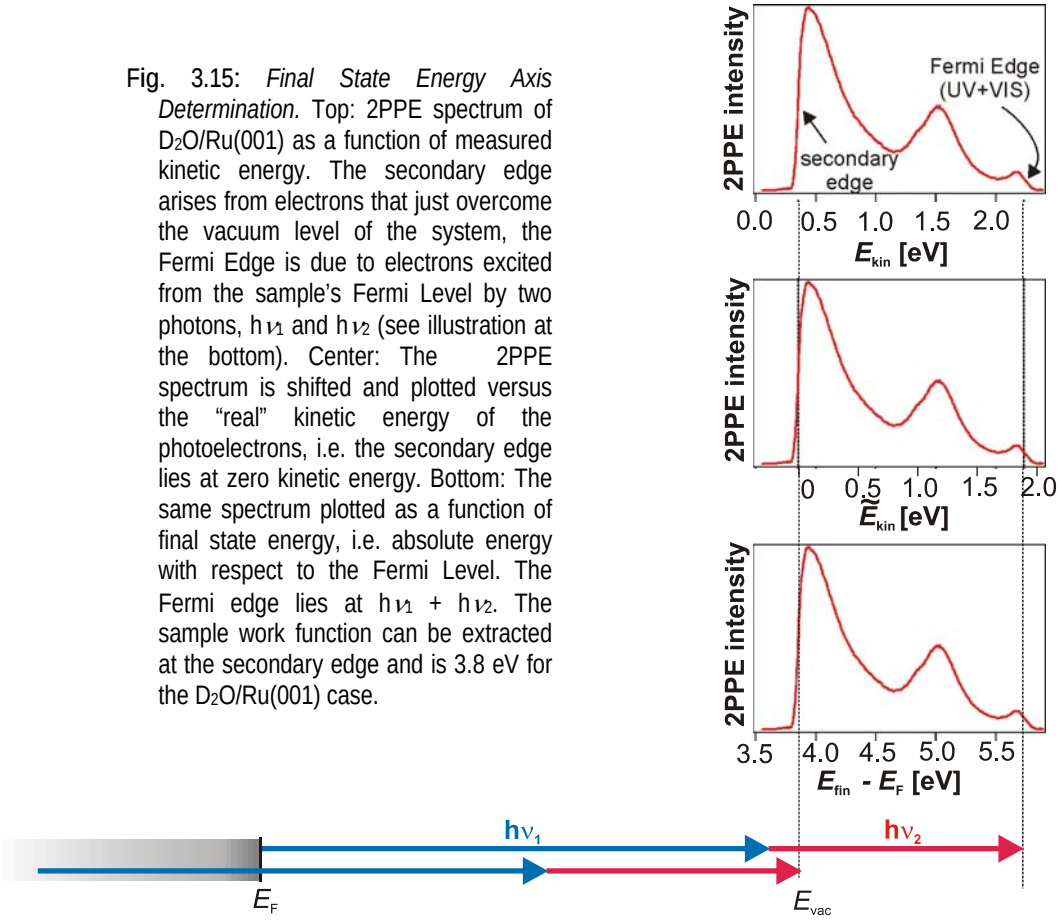

Fig. 3.15: *Final State Energy Axis Determination.* Top: 2PPE spectrum of D_2O/Ru(001) as a function of measured kinetic energy. The secondary edge arises from electrons that just overcome the vacuum level of the system, the Fermi Edge is due to electrons excited from the sample's Fermi Level by two photons, $h\nu_1$ and $h\nu_2$ (see illustration at the bottom). Center: The 2PPE spectrum is shifted and plotted versus the "real" kinetic energy of the photoelectrons, i.e. the secondary edge lies at zero kinetic energy. Bottom: The same spectrum plotted as a function of final state energy, i.e. absolute energy with respect to the Fermi Level. The Fermi edge lies at $h\nu_1 + h\nu_2$. The sample work function can be extracted at the secondary edge and is 3.8 eV for the D_2O/Ru(001) case.

The second fingerprint is due to electrons directly at the Fermi Level that are photoemitted after absorption of the two photons, $h\nu_1$ and $h\nu_2$ (see illustration at the bottom of Fig. 3.15). Note that this spectral feature is termed *Fermi Edge* in the following, while the *Fermi Level* denotes the energy up to which electronic states are occupied at $T = 0$ K. If the 2PPE spectrum is shifted such that the Fermi Edge coincides with the sum of the photon energies (Fig. 3.13, bottom), the spectrum is plotted versus the *final state energy*:

$$E_{fin} - E_F = E_{kin} - E_{kin}(\text{Fermi Edge}) + h\nu_1 + h\nu_2 \tag{3.14}$$

[60] The signal at the secondary edge is mainly due to electrons that have experienced inelastic scattering processes, so-called secondary electrons. Its width is a good measure for the energy resolution of the spectrometer, because it is independent of the spectral width of the laser pulses. For kinetic energies of 0.25 eV, 1 eV, and 3 eV it is 10 meV, 13 meV, and 25 meV, respectively. [Hot99, Gah04]

This energy axis describes the electron energy with respect to the Fermi Level after photoemission. The work function of the sample can be directly extracted from the spectrum at the secondary edge, as the final state energy of the photoelectrons that just overcame E_{vac} is exactly the energy difference between E_F and E_{vac}.

$$\Phi_{sample} = E_{vac} - E_F = E_{fin}(\text{Secondary Edge}) - E_F \tag{3.15}$$

2PPE spectroscopy is primarily employed to investigate intermediate state dynamics. Electron dynamics in final states (i.e. unbound states) are accessible only in special cases. Fig. 3.16 gives an overview of the possible ways to describe the energy of the investigated electronic states between Fermi and vacuum level. The *intermediate state energy* describes the energy with respect to the metal Fermi Level. If the spectral feature is excited by a UV photon, the Fermi Edge of the spectrum has to lie at the energy $h\nu_1$, because the energetically highest signal of electrons excited by UV light is from electrons at the Fermi Level absorbing one UV photon. If the peak of interest results from a VIS excitation, the Fermi Edge lies at $h\nu_2$ (Fig. 3.16, top). Therefore, the intermediate state energy is achieved by (where $h\nu_{pump}$ is the respective pump photon energy):

$$E - E_F = E_{kin} - E_{kin}(\text{Fermi Edge}) + h\nu_{pump} \tag{3.16}$$

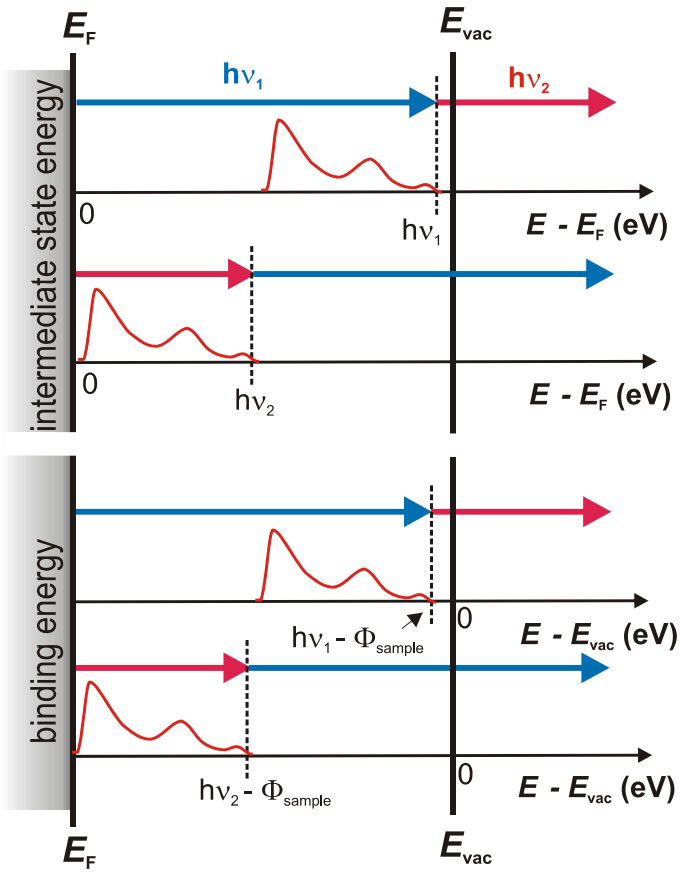

Fig. 3.16: *Energy Axes.* Top: The intermediate state energy with respect to the Fermi Level of electrons excited by UV (VIS) light is defined by a Fermi Edge at $h\nu_1$ ($h\nu_2$). Bottom: The binding energy with respect to the vacuum level for UV- (VIS-) excited electrons is given by an energy axis with the Fermi Edge at $h\nu_1$-Φ_{sample} ($h\nu_2$-Φ_{sample}). See text for details.

As the energetic position of adsorbate-induced features is often quite sensitive to changes of the work function, those spectra are frequently plotted versus *binding energy* with respect to the vacuum level E_{vac} (Fig. 3.16, bottom). As the difference between the Fermi and vacuum level is the system's work function, the binding energy results from

$$E - E_{vac} = E_{kin} - E_{kin}\left(\text{Fermi Edge}\right) + h\nu_{pump} - \Phi_{sample}. \tag{3.17}$$

Besides the intermediate, binding, and final state energies another energy scaling may be useful: The *initial state energy*. If the density of states of the substrate exhibits a maximum below the Fermi Level, 2PPE spectra might exhibit contributions of occupied initial states such as the Cu(111) surface state. To extract the binding energy of such states with respect to the Fermi Level, the spectra are plotted as a function of initial state energy (not shown):

$$E_{ini} - E_F = E_{kin} - E_{kin}\left(\text{Fermi Edge}\right) \tag{3.18}$$

The above discussion illustrates that the knowledge of the character of the investigated spectral features is essential for an appropriate energy axis determination. Whether an observed peak results from an initial, intermediate, or final state and whether it is pumped by either the UV or the VIS laser pulse can be derived unambiguously from photon energy dependent measurements as discussed in section 3.1 or from the temporal evolution of the excited state.

3.4.2 Population Dynamics

To reliably interpret the time-dependence of the 2PPE intensity a basic understanding of the origins is required. The pump laser pulse excites an electron population to an intermediate state. The second (probe) pulse then samples the electron population and leads to the measured 2PPE intensity. However, the description of the electronic excitation using a particle picture (one photon exciting one electron from its ground to its excited state) is rather simple and has to be justified, as – in fact – an oscillating electro-magnetic light field interacts with the electron density of a particular state exhibiting a certain symmetry. The dynamic evolution of the 2PPE intensity is often treated by means of rate equations, which has proven to be appropriate and can be derived theoretically as shown further below. The practical application of these rate equations in fit functions is discussed later.

Einstein Coefficients: The theory of Einstein concerning radiative transitions in two-level systems [Ein17] delivers rate equations for the population of the electronic ground and excited state. Assuming a gas of $N/2$ non-interacting, similar atoms in a cavity, all exhibiting two electronic levels E_1 (ground state) and E_2 (excited state) with the spacing

$$\hbar\omega_0 = E_2 - E_1 \tag{3.19}$$

and a thermal population of the two levels of

$$N = N_1 + N_2, \tag{3.20}$$

three types of different transitions between the states are possible. The spontaneous emission from the excited state to the ground state occurs with the probability A_{21}, absorption of a photon with the probability $B_{12}\langle W(\omega)\rangle$, and stimulated emission with $B_{21}\langle W(\omega)\rangle$. The rate constant of the two latter processes is proportional to the total energy density $\langle W(\omega)\rangle = \langle W_T(\omega)\rangle + \langle W_E(\omega)\rangle$, including the thermal (W_T) and radiative (W_E) contributions. Accordingly, the population change in the excited state is

$$\dot{N}_2 = \frac{dN_2}{dt} = B_{12}\langle W(\omega)\rangle \cdot N_1 - \left(A_{21} + B_{21}\langle W(\omega)\rangle\right) \cdot N_2 , \tag{3.21}$$

where the first term describes the excitation and the second the relaxation contributions.

Bloch Equations: The quantum mechanical approach to the two-level transition is based on the time-dependent Schrödinger equation

$$\hat{\mathcal{H}}(t)\,\Psi(\vec{r},t) = i\hbar \frac{\partial \Psi(\vec{r},t)}{\partial t} \tag{3.22}$$

with the time-dependent Hamiltonian

$$\hat{\mathcal{H}}(t) = \hat{\mathcal{H}}_a(t) + \hat{\mathcal{H}}_I(t) , \tag{3.23}$$

where $\mathcal{H}_a$ describes the time-independent influence of the kinetic and potential energies of the atom constituents and $\mathcal{H}_I$ represents the influence of the incident light with its transient electromagnetic field [Lou00]. The wave function is at all times a linear superposition of the two eigenfunctions Ψ_i, which are normalized and orthogonal:

$$\Psi(\vec{r},t) = C_1(t) \cdot \Psi_1(\vec{r},t) + C_2(t) \cdot \Psi_2(\vec{r},t) \tag{3.24}$$

The expectation value in any of the states described by (3.24) depends on the products of the complex conjugate coefficients C_i. This leads directly to the density matrix ρ_{ij}, described by

$$\rho = \begin{pmatrix} |C_1|^2 & |C_2|^2 \\ C_1 C_2^* & C_2 C_1^* \end{pmatrix} \quad \text{with} \quad |C_i|^2 = \frac{N_i}{N}, \quad i = 1, 2. \tag{3.25}$$

The complex off-diagonal elements describe here the *coherences*, while the diagonal elements are real and describe the *population* of the state |1> and |2>, respectively. The time-dependent changes of the matrix elements are therefore

$$\frac{d\rho_{ij}}{dt} = C_i \cdot \frac{dC_j^*}{dt} + \frac{dC_i}{dt} \cdot C_j^* \ . \tag{3.26}$$

It can be shown [Lou00] that (3.26) results in the *optical Bloch equations*:

$$\frac{d\rho_{22}}{dt} = -\frac{d\rho_{11}}{dt} = -\frac{1}{2} iV\left(\exp\left[i(\omega_0 - \omega)t\right]\rho_{12} - \exp\left[-i(\omega_0 - \omega)t\right]\rho_{21}\right) \tag{3.27a}$$

and

$$\frac{d\rho_{12}}{dt} = -\frac{d\rho_{21}^{*}}{dt} = \frac{1}{2} iV \cdot \exp\left[i(\omega_0 - \omega)t\right] \cdot (\rho_{11} - \rho_{22}), \tag{3.27b}$$

where ω_0 is the energy spacing, ω the frequency of the incident light, and V a scaling factor. (3.27a) simplifies with the substitutions

$$\tilde{\rho}_{12} = \exp\left[i(\omega_0 - \omega)t\right]\rho_{12} \text{ and } \tilde{\rho}_{21} = \exp\left[-i(\omega_0 - \omega)t\right]\rho_{21} \tag{3.28}$$

to

$$\frac{d\tilde{\rho}_{22}}{dt} = -\frac{d\tilde{\rho}_{11}}{dt} = -\frac{1}{2} iV \cdot (\tilde{\rho}_{12} - \tilde{\rho}_{21}) \tag{3.29}$$

For specific boundary conditions the solution of (3.29) has the same analytic form as the rate equation solution for equation (3.21), namely

$$N_2(t) \propto (1 - \exp[-bt]). \tag{3.30}$$

For the bare *population* dynamics only the diagonal elements of the density matrix are important. The solution of (3.29)

$$\tilde{\rho}_{22}(t) = \frac{1}{4} V^2 \left(\frac{\frac{\gamma}{\gamma_{sp}}}{(\omega_0 - \omega)^2 + \gamma^2} + \frac{\frac{2\gamma_{sp} - \gamma}{\gamma_{sp}} \cdot \exp\left[-2\gamma_{sp} t\right]}{(\omega_0 - \omega)^2 + (2\gamma_{sp} - \gamma)^2} - 2\exp[-\gamma t] \times \right.$$
$$\left. \frac{\left[(\omega_0 - \omega)^2 + \gamma(2\gamma_{sp} - \gamma)\right]\cos\left[(\omega_0 - \omega)t\right] + 2(\omega_0 - \omega)(\gamma - \gamma_{sp})\sin\left[(\omega_0 - \omega)t\right]}{\left[(\omega_0 - \omega)^2 + \gamma^2\right]\left[(\omega_0 - \omega)^2 + (2\gamma_{sp} - \gamma)^2\right]} \right) \tag{3.31}$$

with the line width 2γ of the atomic transition and the radiative broadening due to spontaneous emission γ_{sp}, reduces to the form (3.30) if (i) the incident light has a large bandwidth compared with the atomic transition line width or (ii) $\gamma >> \gamma_{sp}$, i.e. the time scale of interest t is on the order of the spontaneous emission time $1/\gamma_{sp}$. [Lou00] In the latter case, which is fulfilled for femtosecond laser pulse excitation, (3.31) reduces to

$$\tilde{\rho}_{22}(t) = \frac{\gamma}{\gamma_{sp}} \cdot \frac{\frac{1}{4} V^2}{(\omega_0 - \omega)^2 + \gamma^2} \cdot (1 - \exp\left[-2\gamma_{sp} t\right]), \qquad \text{for} \qquad \gamma >> \gamma_{sp}. \tag{3.32}$$

Of course, the off-diagonal matrix elements (3.27b), describing the coherences, cannot always be neglected. This assumption is valid only if non-resonant, indirect 2PPE processes are investigated (compare Fig. 3.02). Here, the coherence is lost, so that dephasing effects described by (3.27b) cannot be investigated. This is the case, for example, for the thermalization dynamics of hot electrons close to the Fermi Level. Also, in the case of solvated electrons in adsorbate layers, the off-diagonal elements equal zero: Electrons from below the Fermi Level are excited inside the metal. They transfer into the delocalized conduction band of

the adsorbate layer and localize at favorable sites, which is an inelastic process. In addition, the back transfer occurs via different states in the metal than the excitation, so that all phase information is lost. Hence, the description of the 2PPE data by means of population dynamics only, neglecting the off-diagonal matrix elements, can be applied for solvated electron dynamics. The rate equation approach for the population dynamics investigated here is therefore reasonable.

Fit Functions: Assuming that the collective population dynamics can be described by rate equations as discussed above, the population will follow a function similar to (3.30). The population decay of the excited state may therefore be written as

$$N(t) = A \cdot \exp\left[-\frac{t}{\tau}\right] + B\,, \tag{3.33}$$

where A is the amplitude, τ the decay time and B a constant offset. However, the time-dependent 2PPE intensity is also determined by the pulse duration. To reproduce the data, (3.31) must be convolved with the temporal shape of the laser pulses. It has been shown [Hot99, Gah04, Lis05] that the cross-correlation (XC) of the employed laser pulses is best reproduced by the autocorrelation function of a secans hyperbolicus square (sech^2) function: [61]

$$A_I(t) = \frac{\frac{t}{\tilde{\tau}} \cdot \cosh\left(\frac{t}{\tilde{\tau}}\right) - \sinh\left(\frac{t}{\tilde{\tau}}\right)}{\tilde{\tau} \cdot \sinh^3\left(\frac{t}{\tilde{\tau}}\right)} \tag{3.34}$$

For illustration, Fig. 3.17 shows a fit of the $n = 3$ image potential state of bare Ru(001). The transient XC intensity of the two laser pulses around $E - E_{\mathrm{vac}} = 90$ meV is plotted as a function of pump-probe time delay (markers). Even after 1.5 ps the population of the IPS has not

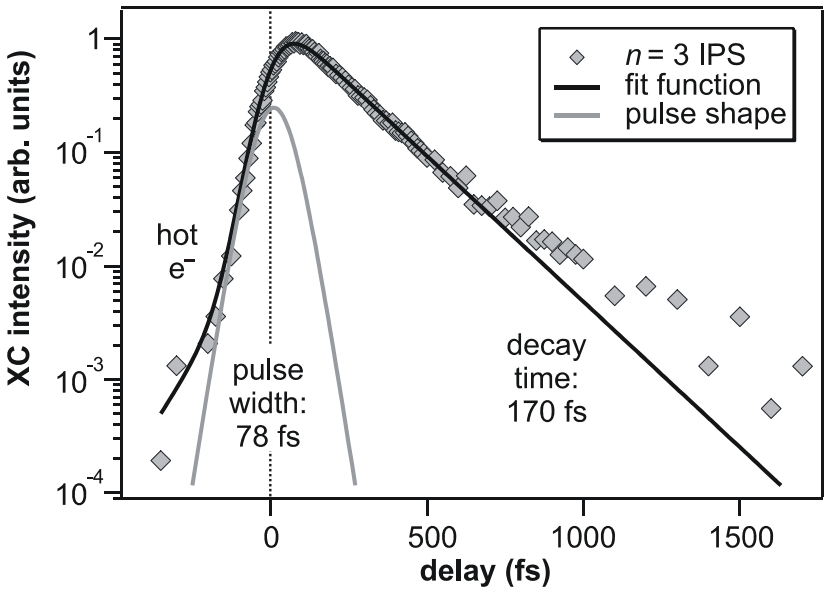

Fig. 3.17: *Single Exponential Fit.* A single exponential decay, convolved with the laser pulses envelope (grey curve), is fitted to the cross correlation trace of the $n = 3$ image potential state of bare Ru(001) (markers). To account for the hot electron dynamics at negative delays, another single exponential is added to the fit function.

decayed completely. The black curve is the least square fit to the data, resulting in a decay time of 170(5) fs. In addition to the decay function (3.33) another term is added to the fit function account for the hot electron signal at negative delays. The total transient population of $n = 3$ and hot electrons is described by

$$\hat{N}(t) = \begin{cases} A \cdot \exp\left[-\frac{t}{\tau}\right] + B & t > 0 \\ A_{HE} \cdot \exp\left[-\frac{t}{\tau_{HE}}\right] & t < 0 \end{cases} \tag{3.35}$$

This expression is convolved with the autocorrelation function of pump and probe pulse laser pulses (grey curve).[62]

To summarize, the basic concept of this data analysis is to define an analytic expression similar to (3.35) that accounts for the population dynamics and to convolve this function with the laser pulses envelope. However, it is shown further below that the population decay of solvated electrons cannot be completely described by this two-level approach with a constant decay time τ. As the solvated electrons subsequently change their degree of confinement and therefore the coupling strength to the metal states, the introduction of energy-dependent transfer times is required (see paragraph 4.1.1). Moreover, for the description of solvated electrons at the NH_3/Cu(111) interface (chapter 5), the implementation of a multi-level system is necessary to reproduce the data.

Outline

The previous chapters summarized the theoretical and experimental background needed for the investigation of the charge transfer and solvation dynamics at D_2O and NH_3 – metal interfaces. In the following, the results for the electron dynamics at these interfaces are presented. Chapter 4 discusses the electron solvation in ice adlayers of various structures and morphologies on two different substrates, developing a consistent picture of electron transfer and solvation at ice-metal interfaces. Chapter 5 presents experiments on amorphous and crystalline ammonia adlayers. The similarities and differences of electron solvation in the two investigated solvents are discussed in detail, showing that thorough knowledge of the underlying processes even enables a tuning of the solvated electron coupling to metal states.

[61] It has to be assumed that the two pulses have the same duration.

[62] At late delays (t > 800 fs) deviations from the exponential decay occur. These are due to intraband scattering processes of the IPS. For details on these electron dynamics at metal surfaces see [Bog04].